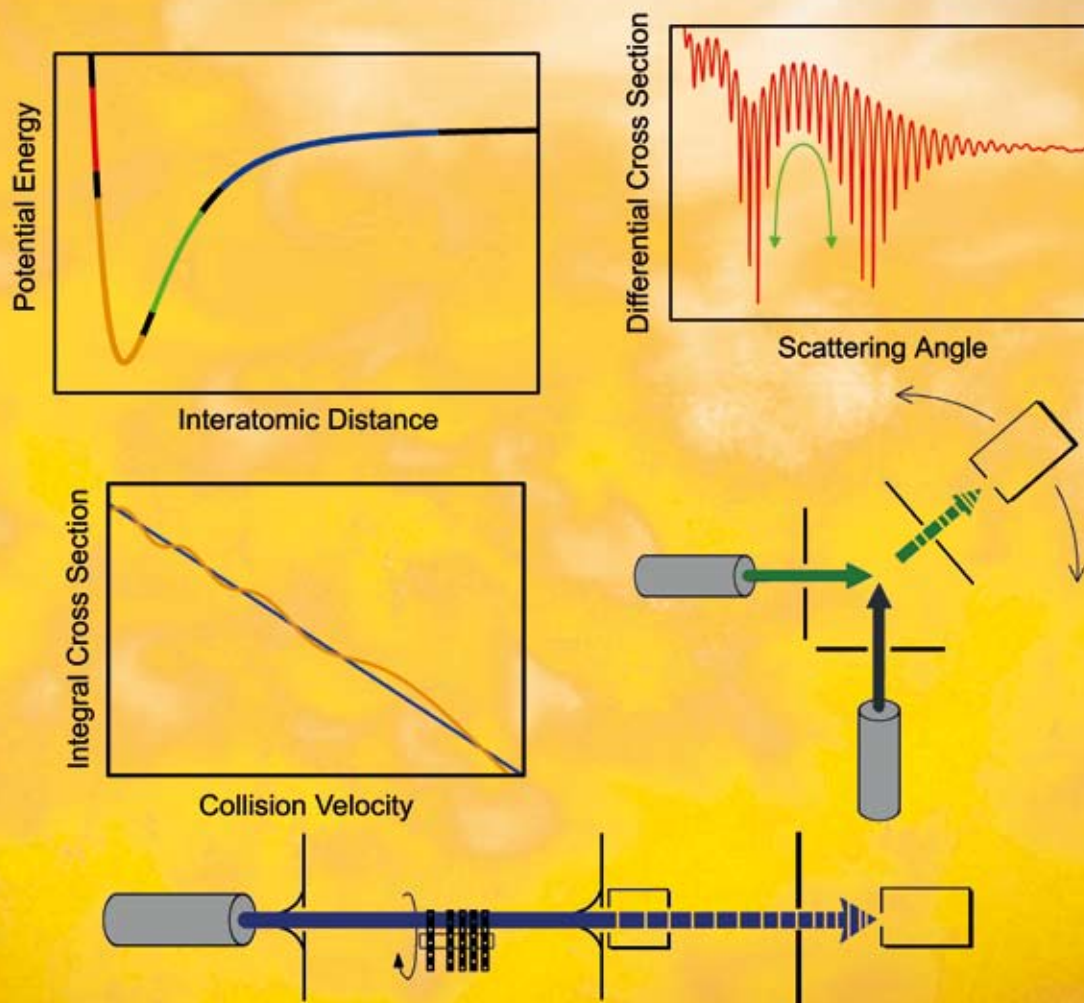


PCCP

Physical Chemistry Chemical Physics

www.rsc.org/pccp

Volume 10 | Number 36 | 28 September 2008 | Pages 5477–5640

**COVER ARTICLE**Pirani *et al.*Beyond the Lennard-Jones model:
a simple and accurate potential function**HOT ARTICLE**Wasylishen *et al.*Solid-state phosphorus-31 NMR
spectroscopy of a multiple-spin system

Beyond the Lennard-Jones model: a simple and accurate potential function probed by high resolution scattering data useful for molecular dynamics simulations

Fernando Pirani,^{*a} Simona Brizi,^a Luiz F. Roncaratti,^a Piergiorgio Casavecchia,^a David Cappelletti^b and Franco Vecchiocattivi^b

Received 20th May 2008, Accepted 19th June 2008

First published as an Advance Article on the web

DOI: 10.1039/b808524b

Scattering data, measured for rare gas–rare gas systems under high angular and energy resolution conditions, have been used to probe the reliability of a recently proposed interaction potential function, which involves only one additional parameter with respect to the venerable Lennard-Jones (LJ) model and is hence called Improved Lennard-Jones (ILJ). The ILJ potential eliminates most of the inadequacies at short- and long-range of the LJ model. Further reliability tests have been performed by comparing calculated vibrational spacings with experimental values and calculated interaction energies at short-range with those obtained from the inversion of gaseous transport properties. The analysis, extended also to systems involving ions, suggests that the ILJ potential model can be used to estimate the behavior of unknown systems and can help to assess the different role of the leading interaction components. Moreover, due to its simple formulation, the physically reliable ILJ model appears to be particularly useful for molecular dynamics simulations of both neutral and ionic systems.

I. Introduction

The equilibrium and non-equilibrium properties of matter, in both gaseous and condensed phases,¹ are mainly determined by the non-covalent intermolecular interactions. Modern molecular dynamics (MD) simulations are of great interest in several applications, including biochemistry and biophysics, since they allow a direct link between macroscopic observables and microscopic intermolecular interactions by using tools of statistical mechanics. However, they require the use of suitable analytical functions, representing the dependence of the potential energy V on the separation distance r and relative

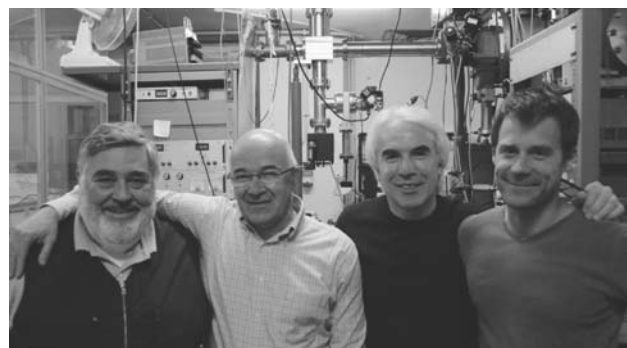
orientation of the interacting partners. This request arises from the necessity to easily obtain the involved force field. Often, the limiting factor in the ability of these computations to describe real systems is the lack of a realistic description of the intermolecular interaction potential energy. The simple Lennard-Jones potential model is extensively used in MD simulations, but this model is known to exhibit some inadequacies at short and large intermolecular distances.

This perspective article focuses on the detailed characterization and modeling of V associated to non-covalent intermolecular interactions, and proposes the adoption of a simple, yet physically accurate, potential model readily usable for molecular dynamics simulations of both neutral and ionic systems of increasing complexity.

An important contribution to the non-covalent interactions comes from the van der Waals component, V_{vdW} , here defined

^a Dipartimento di Chimica, Università di Perugia, 06123 Perugia, Italy. E-mail: pirani@dyn.unipg.it

^b Dipartimento di Ingegneria Civile e Ambientale, Università di Perugia, 06125 Perugia, Italy



F. Vecchiocattivi, F. Pirani, P. Casavecchia and D. Cappelletti

Professors F. Pirani, F. Vecchiocattivi, D. Cappelletti and P. Casavecchia are members of the Collision Dynamics group in Perugia. L. Roncaratti and S. Brizi are current and former students of the group, respectively. The research interests of Pirani, Vecchiocattivi and Cappelletti are focused on the determination of intermolecular potentials via integral cross section measurements and on the development of correlation formulae with predictive power. Their current interests also include alignment effects, gas-surface interactions, solvation phenomena and photoionization processes studied with synchrotron light. The research interests of Casavecchia were centered on intermolecular potentials via high-resolution differential cross section measurements, before he moved on to reactive scattering and reaction dynamics, for which he has received the 2008 Polanyi Medal.

as the combination of the short-range exchange (or size) repulsion with the long-range dispersion attraction. The V_{vdw} component, always present in every system, is often not accurately described.

The rare gas dimers are prototypical systems where the interaction potential is exclusively a pure V_{vdw} . In the past, these systems have been extensively investigated. In particular, collisional cross sections (see, for instance, ref. 2–6), transport properties (see ref. 1 and 7) and spectroscopic data (see ref. 8–13) have been measured. For a detailed description of the knowledge of the rare-gas two-body interatomic potentials up to the 1980s, see ref. 14 and 15. The combined analysis of experimental data of different types (usually referred to as multiproperty analysis) has often been performed by using empirical functions to describe V_{vdw} . In particular, flexible and multiparameter models, such as Morse–Spline–van der Waals (MSV),¹⁶ Exponential-Spline–Morse–Spline–van der Waals (ESMSV)² and Simons–Parr–Finlan (SPF) modification of the Dunham expansion,^{17–19} have been widely used (further empirical functions are given in ref. 1). Some important semi-empirical models have also been introduced which appear to be reliable in a wide r range; they describe the potential function, in the region around the equilibrium distance, as the combination of two functions, representing the short-range repulsion and the long-range damped dispersion attraction. In particular, the Hartree–Fock–Dispersion (HFD)^{20,21} model and its modifications^{22–25} have been extensively used over the last 25 years. Another important model has been proposed by Tang and Toennies (TT),²⁶ which has also been extended to systems involving ions²⁷ and diatomic molecules.²⁸ In the TT model, the short-range repulsive Born–Mayer potential is added to the long-range attraction, represented again by a selectively damped dispersion/induction series.

The empirical and semiempirical models mentioned above exhibit some difficulties in their extension and generalization to more complex cases (*i.e.* beyond the closed shell atom-closed shell atom systems) because they involve too many parameters, some not easily and directly obtainable. Moreover, their first and second derivatives can show discontinuities, especially at the joining points of the different analytical functions involved.

As stressed above, most of modern MD simulations still extensively use the venerable Lennard-Jones (LJ) function (first suggested by Mie in 1903 and later adopted by Lennard-Jones²⁹), since it requires only a few parameters and exhibits a simple formulation with analytical first and second derivatives. Such a model has also been often used in the study of scattering processes and in the analysis of the experimental scattering results. However, it is well known that although the LJ model almost accurately reproduces the main features of the interaction around the equilibrium distance (the so called potential well that occurs at intermediate r) it overestimates the strength of both the long-range attraction and the short-range repulsion.

The main purpose of this article is to demonstrate that a potential function, recently introduced to represent in a suitable form the interaction in systems involving aliphatic and aromatic hydrocarbons,³⁰ is able to simultaneously describe a very large body of experimental data. These data are: rare gas atom-rare gas atom scattering cross sections, obtained in

our laboratory (some already published and some new) and in Leiden, transport properties and spectroscopic information on the same systems. This model, which is an extension and generalization of a potential function proposed by Maitland and Smith,³¹ involves only one additional parameter with respect to the venerable LJ function; for this reason it has been called “Improved Lennard-Jones” (ILJ). The ILJ exhibits analytical and continuous first and second derivatives and, in addition, its parameters can be predicted by scaling laws based on the use of fundamental physical properties of the interacting partners.³² Moreover, its short-range wall is less repulsive with respect to that of LJ and its long-range behavior appears to be quite reliable. In fact it reproduces the absolute value of the measured integral cross section and asymptotically provides, differently from the LJ model, an induced dipole-induce dipole constant (C_6) in quite reasonable agreement (within 10–15%) with the theoretical values.

It should be noted that the purpose of this article is not that of providing the characteristics of V_{vdw} for the rare gas dimers with improved accuracy, since they are already well known¹⁵ (the current situation has been reviewed in a recent paper³³). Rather, this article presents a detailed test of a simple potential model, the ILJ, which can be readily applied to a large variety of systems. Indeed, it will be demonstrated that this model permits us to cover a wide phenomenology associated with the non-covalent intermolecular interactions in systems of increasing complexity, both neutral and ionic.

In section II the main features of the experimental apparatuses, that have been used to obtain the new scattering data, are summarized. Section III emphasizes the dependence on the features of the interaction potential of quantum interference effects, observable in scattering experiments in the thermal energy range. Section IV discusses the functional form of the ILJ potential model. Section V describes the analysis of integral and differential cross section data measured in our laboratory. In section VI the analysis is also extended to the experimental data obtained by the Leiden group.^{34,35} Discussion is presented in section VII, while conclusions follow in section VIII.

II. Experimental apparatuses

The integral cross section $Q(v)$, as a function of the collision velocity v , and the differential cross section $I(\theta)$, at a defined collision energy E and as a function of the laboratory scattering angle θ , measured in our laboratory and here analyzed, have been obtained in two different molecular beam apparatuses operating in Perugia. They consist of sets of differentially pumped vacuum chambers, where the molecular beams are collimated by appropriate slits and the experiments are carried out under high-resolution conditions, both in energy and angle. This allows the observation of quantum interference effects, such as the glory structure in the integral cross section and the rainbow and diffraction oscillations in the differential cross section. In both apparatuses, the detector consists of a quadrupole mass spectrometer with an electron bombardment ionizer. Details about these apparatuses have been given in previous papers (see for instance ref. 36–39). A sketch is shown in Fig. 1, where panels (a) and (b) schematize the measurement

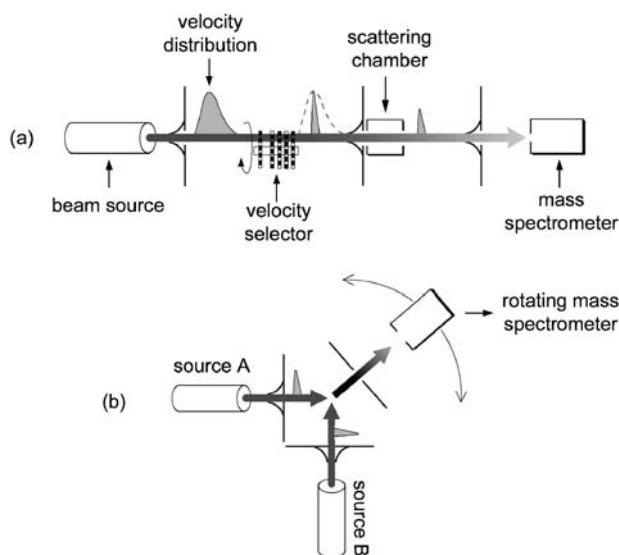


Fig. 1 Sketch of the experimental apparatuses used to measure integral (a) and differential (b) cross sections.

principle of $Q(v)$ and $I(\theta)$, respectively. In Table 1 some operating conditions, of relevance for the experiments presented here, are listed.

$Q(v)$ is obtained from the beam attenuation I/I_0 (where I and I_0 represent the beam intensity with and without the target gas in the scattering chamber) measured at the selected beam velocity v , and by applying the Lambert-Beer law. The use of an internal flow calibration for the gas density and of a reference cross section permits the assessment of the obtained $Q(v)$ in an absolute scale of values, with an uncertainty estimated to be not larger than 3–4% (see ref. 37 and references therein). In all cases, the scattering chamber is cooled to 90 K, in order to increase the velocity resolution of the

experiment. The stationary pressure of the target has been fixed at a sufficiently low value (particularly for Xe) in order to make dimer formation negligible.⁴⁰ Recently, $Q(v)$ measurements have been performed in an extended range of selected beam velocity v by exploiting new beam sources (operating at a controlled temperature) and a new velocity selection device, formed by six rotating slotted thin disks and having a resolution power better than 5% (full width at half maximum).

The differential cross sections have been measured by using a high-resolution crossed molecular beam apparatus³⁸ (see panel (b) of Fig. 1) with beam sources operating at nearly room temperature. Briefly, two well collimated, doubly differentially pumped, supersonic nozzle beams are crossed at 90° in a large scattering chamber kept at 10^{-7} mbar in operating conditions. The in-plane scattered lighter particle (Ne atom) is detected by a rotatable triply differentially pumped ultra-high-vacuum quadrupole mass-spectrometer detector maintained in the 10^{-11} mbar pressure range in the ionization region by extensive ion-, turbo-, and cryo-pumping. Since the absolute accuracy of the measurements depends on the calibration of the velocity distributions of the two beams, as well as of the angular positions, great care was devoted to all these aspects. The beam velocities were measured by absolute time-of-flight analysis to better than 0.6%, the angular locations were determined to better than 0.03°, and the geometrical alignments were carried out to within 0.05 mm. While the primary beam (Ne) was produced by high-pressure expansion to achieve a high speed ratio ($s = 36$), the secondary Ne, Ar, Kr and Xe beam pressures were chosen as to give the maximum signal intensity while avoiding possible problems from condensation effects (see Table 1). The secondary beam was modulated at 160 Hz for background subtraction.³⁸ The detector angular resolution was set to 0.5° for a point collision zone. The same geometrical arrangement was maintained for all systems, and this permits us to put on a very precise relative basis the different results.

Table 1 Typical operating conditions in the molecular beam experiments

Apparatus for $Q(v)$ measurements (see panel (a) in Fig. 1)	
Beam source	
Nozzle diameter/mm	1.0
Stagnation pressure/mbar	3–30
Scattering chamber	
Temperature/K	90
Target pressure range/mbar	10^{-2} – 10^{-3}
Target density/molecule cm^{-3}	10^{14} – 10^{15}
Scattering path length/cm	~ 7
Beam angular divergence/rad.	$\sim 10^{-3}$
Velocity resolution (fwhm)	5%
Apparatus for $I(\theta)$ measurements (see panel (b) in Fig. 1)	
Primary beam source (Ne)	
Nozzle diameter/mm	0.025
Stagnation pressure/bar	18
Peak velocity/ m s^{-1}	797
Beam velocity spread $\Delta v/v$ (fwhm)	4.6%
Beam angular divergence/°	0.4
Secondary beam source (Ne, Ar, Kr, Xe)	
Nozzle diameter/mm	0.10
Stagnation pressure/bar	1.8–0.5
Nozzle temperature/K	304–306
Peak velocity/ m s^{-1}	797–561–388–310
Beam velocity spread $\Delta v/v$ (fwhm)	9.1–9.8%
Beam angular divergence/°	1.8

III. Scattering observables and interaction potential

The dependence of elastic scattering observables on the features of the interaction potential has been extensively described and discussed in the literature (see ref. 1,41–43 and references therein). Here we only stress some general and basic aspects, which are of interest to the present study. Panel (a) of Fig. 2 defines the main features of the interaction potential energy V when reported as a function of the interatomic distance r . Panel (b) shows the general behavior, in the center-of-mass system, of the differential cross section exhibiting diffraction and rainbow oscillations. Panel (c) reports the behavior of the integral cross section $Q(g)$ as a function of the relative collision velocity g . As usual, $Q(g)$ is plotted (panel (d)) as $Q(g)g^{2/5}$ to emphasize the glory structure and to separate the glory pattern $\Delta Q(g)$ from the smooth component $\bar{Q}(g)$. It was also demonstrated⁴¹ that there is a direct correlation between the number of glory extrema and the number of vibrational states supported by V (see insert in panel (c)). Fig. 2 also gives evidence of the dependence of $\Delta Q(g)$ and $\bar{Q}(g)$ from the potential well features (essentially the depth ε and the equilibrium distance r_m) and from the long-range

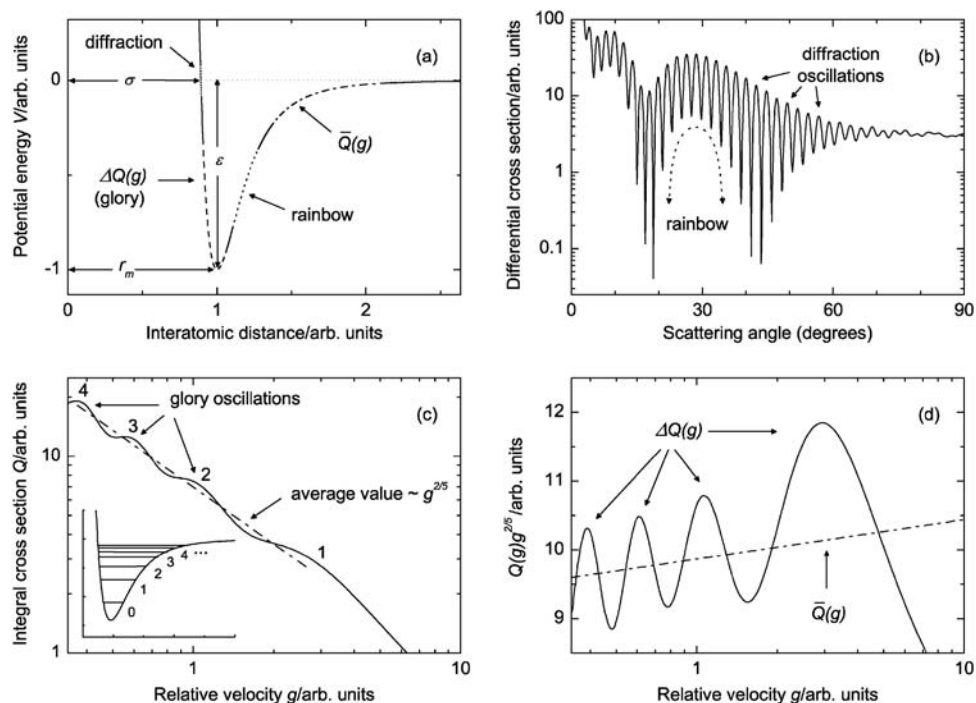


Fig. 2 Specific features of the interaction potential energy V and their relation with the center of mass scattering observables. Simulations are performed on the Ar–Ar system (for more details on V see text).

attraction. We recall that the glory frequency and amplitude depend, respectively, on the product ϵr_m and on the potential well shape in the interval $\sigma < r \leq r_m$, while the absolute value of the integral cross section is the only direct probe of the long-range potential.^{41,44} In the same figure the dependence of rainbow and diffraction effects, respectively from the attraction in the proximity of the well (affected by the ϵ value) and from the position of the repulsion onset (defined by σ , *i.e.* by the distance where the inner zero of V occurs), is also illustrated. We recall that the rainbow scattering angle is probably the most direct and unique measure of the potential well depth ϵ , while the diffraction oscillations give us a direct measure of the diameter σ of the repulsive wall (and indirectly of the minimum position r_m).⁴³

Symmetry effects are observable in the scattering of identical collision partners. They provide further information on the interaction potential. For light systems, colliding at thermal energies, such additional information mostly concerns the onset of the repulsive branch of the potential energy curve.⁴³

A partial-wave analysis of the quantum mechanical scattering helps to make some of these aspects more quantitative. Following this analysis, the integral cross section Q can be conveniently interpreted as a sum of partial-wave contributions Q_ℓ :

$$Q(g) = \sum_{\ell=0}^{\infty} Q_\ell \quad (3.1)$$

where each Q_ℓ , depending on the ℓ th phase shift, probes a specific range of r . This range is located in the neighborhood of the turning point $r_c(\ell)$, that corresponds, in a classical description, to the distance of closest approach, where most of the phase shift is accumulated. In particular it occurs for $r \gtrsim r_c$.

Fig. 3 and 4 illustrate the behavior of two systems (He–Xe and Ar–Ar), which will be more extensively discussed in the following sections. In particular, Fig. 3 shows, for He–Xe, the behavior of Q_ℓ at two collision velocities, higher than that corresponding to the first glory maximum. In these conditions the $Q(g)$ values probe the whole potential well, while further

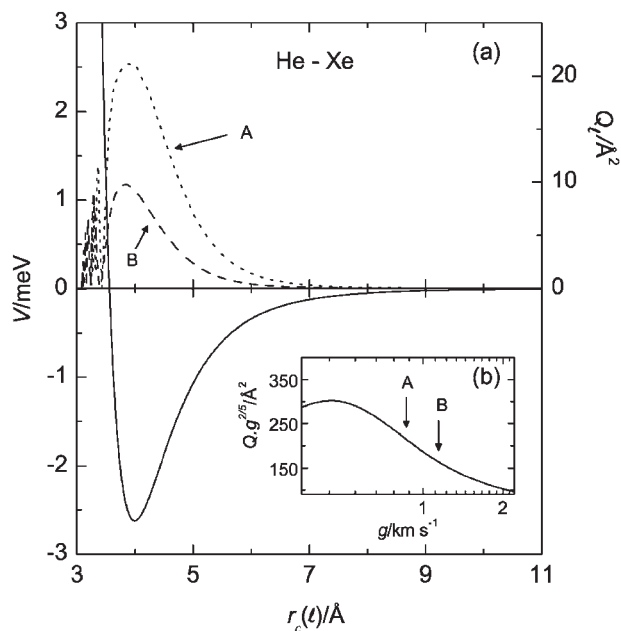


Fig. 3 The interaction potential for the He–Xe system (continuous line). Dashed and dotted lines represent partial contributions Q_ℓ as a function of the classical turning point $r_c(\ell)$ for two different collision velocities, as indicated in the insert.

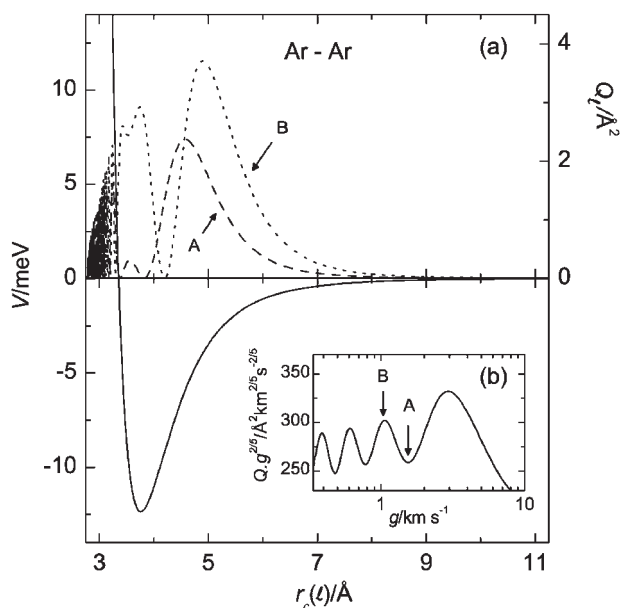


Fig. 4 The interaction potential for Ar–Ar system (continuous line). Dashed and dotted lines represent partial contributions Q_r as a function of the classical turning point $r_c(l)$ for two different collision velocities, as indicated in the insert.

increasing g , Q tends to be mostly affected by the repulsive wall. Fig. 4 reports, for the Ar–Ar system, Q_r at two collision velocities, corresponding to a maximum (an order of 2) and a minimum (an order of 1.5) glory extremum, respectively. Two relevant contributions are observable: the first one, affected by V at $r \lesssim r_m$, appears to be strongly varying with g and provides $\Delta Q(g)$; the second contribution, affected by the long-range attraction and smoothly varying with g , determines $\bar{Q}(g)$.

IV. The potential model

The ILJ potential model has the general form

$$V(r) = \varepsilon \left(\frac{m}{n(r) - m} \left(\frac{r_m}{r} \right)^{n(r)} - \frac{n(r)}{n(r) - m} \left(\frac{r_m}{r} \right)^m \right), \quad (4.2)$$

where ε and r_m , respectively, represent the depth of the potential well and its location (see panel (a) of Fig. 2), while r/r_m is the reduced distance. In ref. 30 this potential function was denoted as $[n(x), m]$, but for the considerations given below the terminology ILJ appears to be more appropriate. In eqn (4.2) the first term describes the r -dependence of the repulsion, while the second one represents the r -dependence of the long-range attraction. The exponent in the second term assumes the value $m = 6$ for all neutral–neutral systems, whereas it becomes $m = 4$ for ion–neutral and $m = 1$ for ion–ion cases. The $n(r)$ term depends on r as

$$n(r) = \beta + 4 \left(\frac{r}{r_m} \right)^2. \quad (4.3)$$

β is a factor related to the hardness of the two interacting partners and is expected to vary in a limited range, when passing from one system to another, following some trends and regularities. If n is assumed to be independent of r , the

eqn (4.2) becomes identical to the usual LJ(n, m) model. From eqn (4.3) we can see that $n(r \rightarrow \infty) \rightarrow \infty$ and $n(r \rightarrow 0) \rightarrow \beta$. It follows that the asymptotic dipole–dipole C_6 constant for neutral–neutral systems assumes the form εr_m^6 , while the asymptotic charge–induced dipole C_4 constant, for ion–neutral systems, becomes εr_m^4 and the C_1 constant, for ion–ion systems, is εr_m . Moreover, the combined effect of β and m defines the reduced force constant³⁰ and the stretching frequency of the interacting system. The values of these quantities at r_m are of particular interest.³³

Therefore, as discussed below, the $n(r)$ dependence leads to a correct representation of the long-range attraction and attenuates the hardness of the repulsive wall, as r decreases, with respect to that provided by the usual LJ model. As stressed in the introduction, such a formulation of the interaction represents an extension and a generalization of a model presented several years ago by Maitland and Smith³¹ for neutral–neutral systems and which has been successfully tested on thermo-physical properties of rare gases (see also ref. 45).

The use of only three parameters, ε , r_m and β (the latter to be kept variable only within a restricted range of values) allows the ILJ model to reproduce the $V(r)$ behavior both in the negative region of the interaction and in the onset of the positive part where the repulsion starts. This aspect will be analyzed in detail in the following sections.

V. Analysis of integral and differential cross sections

In this section we report new scattering data for some rare gas systems, that have been measured by using the apparatuses schematized in Fig. 1 and described in section II. In some cases, these data are combined in a multiproperty analysis with old results, that we have previously obtained. For the He–Xe and Ne–Xe systems, we have recently performed new integral cross section experiments in an extended v range, by using He and Ne beams scattered by Xe target atoms. For the analysis of $Q(v)$ for Ne–Ne, Ne–Ar and Ne–Kr systems, we use data from our laboratory previously published.^{4,6,46,47} Concerning the differential cross sections $I(\theta)$ for Ne–Ne, Ne–Kr and Ne–Xe, we use results measured with the apparatus schematized in the lower panel of Fig. 1. For Ne–Ar, data already published⁴⁸ are reanalyzed. For each system, the data analysis has been performed by using the ILJ model, where the β parameter (see eqn (4.3)) has been fixed to $\beta = 9$ in all cases. The results are compared to those obtained by using the familiar LJ(12,6) model with the same ε and r_m involved in ILJ. Cross section calculations have been also performed by using for the same systems the HFD potentials proposed in the literature. The ε , r_m and σ values, associated to the different potentials are listed in Table 2, where predictions from correlation formulae^{49,50} given in terms of polarizabilities of the interacting partners, are also reported for comparison. These correlation formulae, of general validity for V_{vdw} , provide an estimate of ε (within 10–15%) and r_m (within 3–5%) values for any type of system, while the present best-fit ε and r_m have a maximum uncertainty of 2–3% (4% for He–Xe) and 0.6%, respectively.

Integral and differential cross sections, calculated in the center of mass (CM) system, are then convoluted in the laboratory (LAB) frame in order to make a direct comparison with the experimental data. Calculated results are obtained by evaluating the phase-shifts within the JWKB approximation, and applying the JB scheme at large values of ℓ .^{1,41}

A He–Xe

$Q(v)$ data are plotted in panel (a) of Fig. 5 as a function of the selected He beam velocity v . In panel (b) of the same figure the first low velocity points are plotted as $Q(v)v^{2/5}$ to emphasize the observation (never previously reported) of the glory extremum of order 1 (see panel (c) of Fig. 2). For this system Danielson and Keil⁵¹ and Aziz *et al.*⁵² provided high-resolution differential cross sections, in which well resolved

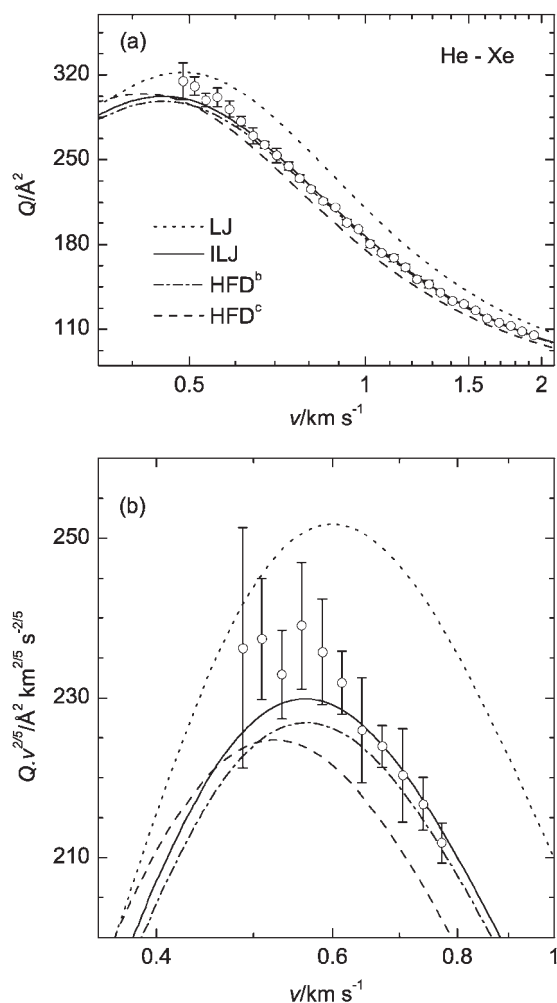


Fig. 5 Integral cross sections $Q(v)$, measured as a function of the He beam velocity v , and comparison with calculations by using different potential models. The full line represents the best-fit obtained by using ILJ, dotted, dashed–dotted and dashed lines are obtained by using LJ, HFD^b and HFD^c potential models (see text and Table 2). Panel (a) plots $Q(v)$ as a function of the beam velocity v . The experimental data are lowered (within the uncertainty concerning the calibration of the absolute scale) of about 2%. In panel (b) the first eleven experimental points are plotted as $Q(v)v^{2/5}$ to emphasize the observation of the first glory maximum.

Table 2 Well depth ε , equilibrium distance r_m and zero of the potential σ for the different potentials models. Predictions of correlation formulas are also reported for comparison

System	Potential	ε/meV	$\sigma/\text{\AA}$	$r_m/\text{\AA}$
He–Xe	ILJ	2.624	3.562	3.994
	LJ	2.624	3.558	3.994
	Predicted ^a	2.84		3.93
	HFD ^b	2.635	3.565	3.997
	HFD ^c	2.495	3.547	3.975
Ne–Ne	ILJ	3.660	2.759	3.094
	LJ	3.660	2.756	3.094
	Predicted ^a	4.28		3.10
	HFD-B ^d	3.638	2.759	3.091
	ILJ	5.740	3.139	3.520
Ne–Ar	LJ	5.740	3.136	3.520
	Predicted ^a	5.74		3.52
	HFD-B ^e	5.819	3.114	3.489
	ILJ	6.160	3.264	3.660
	LJ	6.160	3.261	3.660
Ne–Kr	Predicted ^a	6.25		3.70
	HFD-B ^f	6.163	3.249	3.621
	ILJ	6.350	3.464	3.885
	LJ	6.350	3.461	3.885
	Predicted ^a	6.17		3.93
Ne–Xe	HFD-B ^f	6.389	3.465	3.861

^a Ref. 49 and 50. ^b Ref. 51. ^c Ref. 52. ^d Ref. 53. ^e Ref. 54. ^f Ref. 55.

diffraction oscillations were observed. The present analysis has been preliminarily performed by using the two HFD potential models proposed in ref. 51 and 52 and Fig. 5 reports the $Q(v)$ calculations (dashed–dotted lines and dashed lines). The comparison indicates that the predictions of both potentials are in reasonable agreement (almost within the experimental uncertainty) with the measured data.

The best-fit of $Q(v)$ is achieved by using the ILJ model, where the r_m parameter has been taken within the values of the two HFD models. The well depth ε has been varied in order to reproduce the experimental behavior (full line in Fig. 5) and the parameters are given in Table 2. A calculation has also been performed with the LJ potential (see Table 2 and dotted lines in Fig. 5) which provides $Q(v)$ values that are too large with respect to the experimental ones, indicating that the negative area of the LJ model is too wide (too strong an attraction).

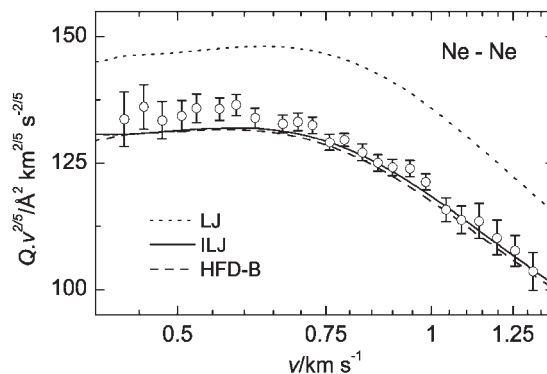


Fig. 6 Integral cross sections $Q(v)$, measured as a function of the Ne beam velocity v , and comparison with calculations using the HFD, ILJ and LJ models (see also Table 2). The experimental data are lowered of about 4%, still within the uncertainty concerning the calibration of the absolute scale.

B Ne–Ne, Ar, Kr and Xe

The Ne–Ne system has been investigated by simultaneously analyzing some previously published $Q(v)$ data,^{4,46} reported in Fig. 6, and new $I(\theta)$ results, reported in Fig. 7. In the latter case, two crossed supersonic beams (see panel (b) of Fig. 1) of natural neon have been employed and the detection of scattered atoms has been selectively performed on the masses of ^{20}Ne and ^{22}Ne . In this way, the symmetry and diffraction oscillatory patterns have been clearly distinguished by performing isotope resolved angular distribution measurements. From the relative populations of the two main isotopes in natural Ne (91% of ^{20}Ne and 9% of ^{22}Ne) it follows:

$$I(^{20}\text{Ne}) = 0.91I(^{20}\text{Ne}-^{20}\text{Ne}) + 0.09I(^{20}\text{Ne}-^{22}\text{Ne})$$

$$I(^{22}\text{Ne}) = 0.09I(^{22}\text{Ne}-^{22}\text{Ne}) + 0.91I(^{22}\text{Ne}-^{20}\text{Ne}). \quad (5.4)$$

When detecting ^{20}Ne the observed $I(\theta)$ exhibits closely spaced, yet well resolved, diffraction oscillations at small angles and very pronounced symmetry oscillations at large angles. In the

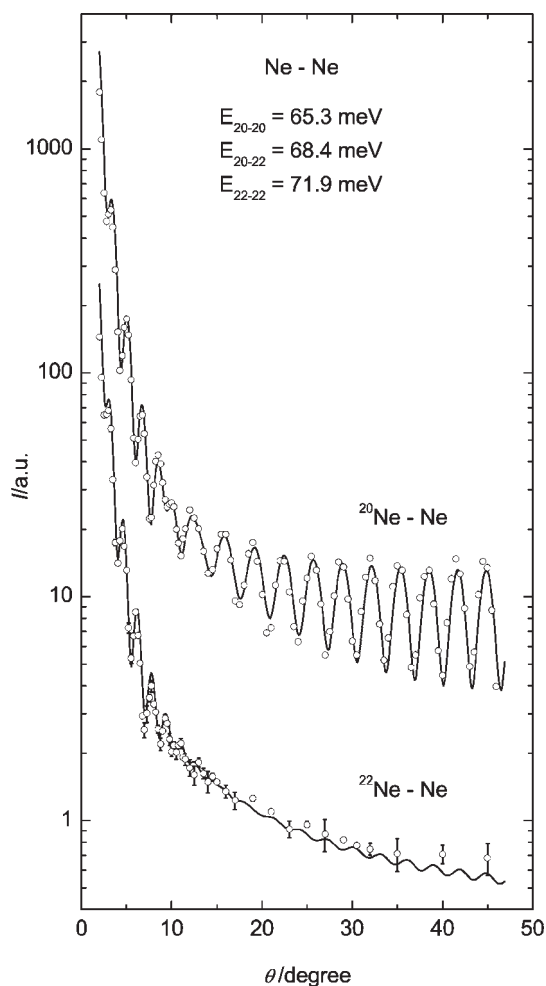


Fig. 7 Differential cross section $I(\theta)$ measured as a function of LAB scattering angle θ , obtained detecting ^{20}Ne and ^{22}Ne scattered particles. The different collision energies E for the three different isotopes pairs are also reported. Error bars (± 1 standard deviation) are indicated when visible outside the experimental dots. Calculations with the various potential models (see text) are indistinguishable within the line size.

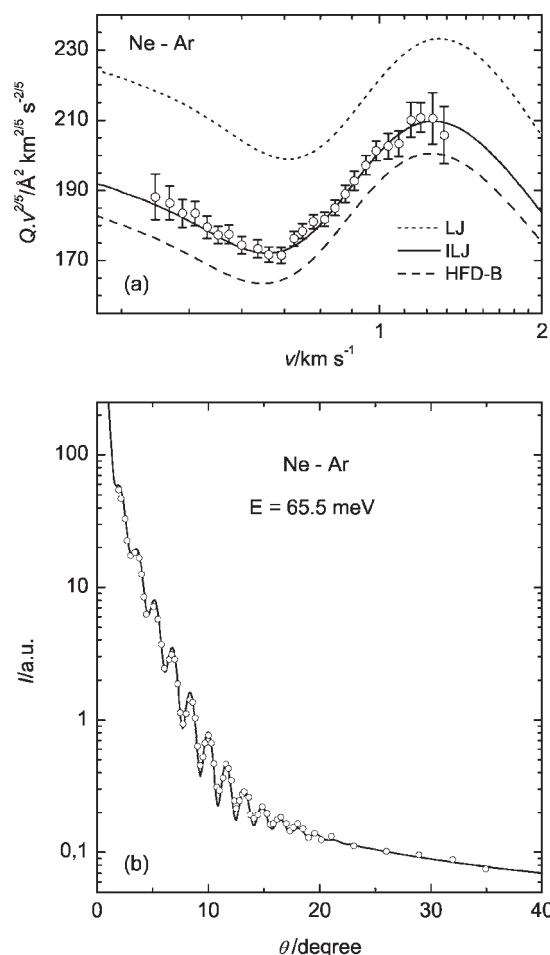


Fig. 8 Integral cross sections $Q(v)$ (upper panel), measured as a function of the Ne beam velocity v , and comparison with calculations using the HFD, ILJ and LJ models (see also Table 2). Differential cross section (lower panel) $I(\theta)$, measured at the indicated collision energy E and as a function of LAB scattering angle θ . Error bars are smaller than the experimental dots. Calculations of $I(\theta)$ (full line) with the three potential models (see text) are indistinguishable within the line size.

integral cross section (Fig. 6), symmetry effects are much smaller in the CM because of the combined effect of several partial waves and are completely smoothed by the convolution in the LAB system. When detecting ^{22}Ne , the symmetry structure is not present any more in the observed $I(\theta)$, mostly affected by $I(^{22}\text{Ne}-^{20}\text{Ne})$. However, the calculated $I(\theta)$ still exhibits some symmetry oscillations due to $^{22}\text{Ne}-^{22}\text{Ne}$ scattering (which accounts for about 9% of total signal) superimposed to the smooth $^{22}\text{Ne}-^{20}\text{Ne}$ scattering, but this damped structure is not resolved experimentally because of the lower signal/noise ratio when detecting ^{22}Ne .

The simultaneous analysis has been carried out again by using the previously proposed HFD-B model,⁵³ ILJ and LJ. For this system the HFD-B and ILJ models provide a nearly indistinguishable fit of the experimental data, while LJ overestimates the $Q(v)$ value since its long-range attraction is too strong and makes the $\bar{Q}(v)$ component too large (see Fig. 6).

In the past, we have investigated the Ne–Ar system.^{47,48} Here it is reanalyzed (see Fig. 8) using the HFD-B,⁵⁴ ILJ and

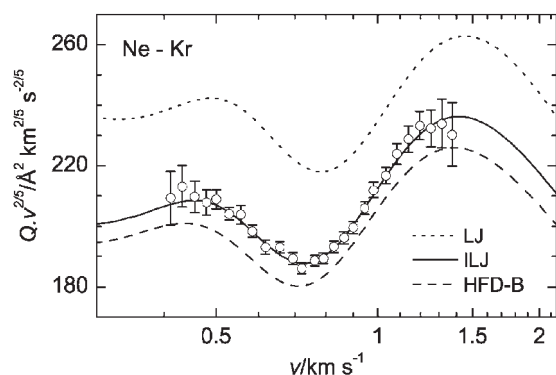


Fig. 9 Integral cross sections $Q(v)$, measured as a function of the Ne beam velocity v , and comparison with calculations using the HFD, ILJ and LJ models (see also Table 2). The experimental data are lowered of about 1%, still within the uncertainty concerning the calibration of the absolute scale.

LJ potential models, in order to have a set of internally consistent parameters (see Table 2 for the comparisons). LJ provides a slight shift of the glory extrema position and overestimates $\bar{Q}(v)$ because its attraction is too strong (see also the Ne–Ne case presented above), while $\bar{Q}(v)$ provided by the HFD-B model is lower (by 5%) than the experimental one, slightly outside the lower limit of the experimental uncertainty.

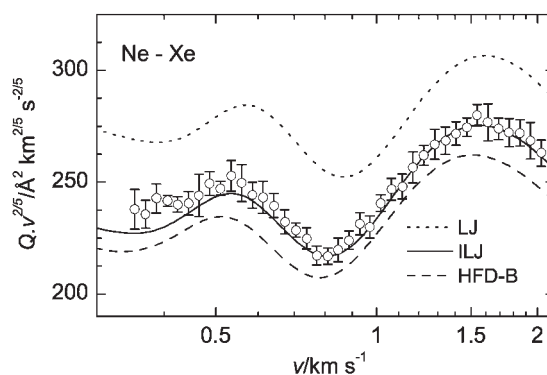


Fig. 11 Integral cross sections $Q(v)$, measured as a function of the Ne beam velocity v , and comparison with calculations using the HFD, ILJ and LJ models (see also Table 2). The experimental data are lowered of about 4%, still within the uncertainty concerning the calibration of the absolute scale.

For the Ne–Kr system, during the analysis the experimental $I(\theta)$ data have been combined with some old $Q(v)$ data. Fig. 9 shows the comparison between the measured $Q(v)$ and calculations carried out with HFD-B,⁵⁵ LJ and the best-fit ILJ model. In Fig. 10, $I(\theta)$ values are plotted as $I(\theta)\theta^{7/3}$, which emphasizes the rainbow structure superimposed with the diffraction oscillations. The HFD-B model provides $Q(v)$ with

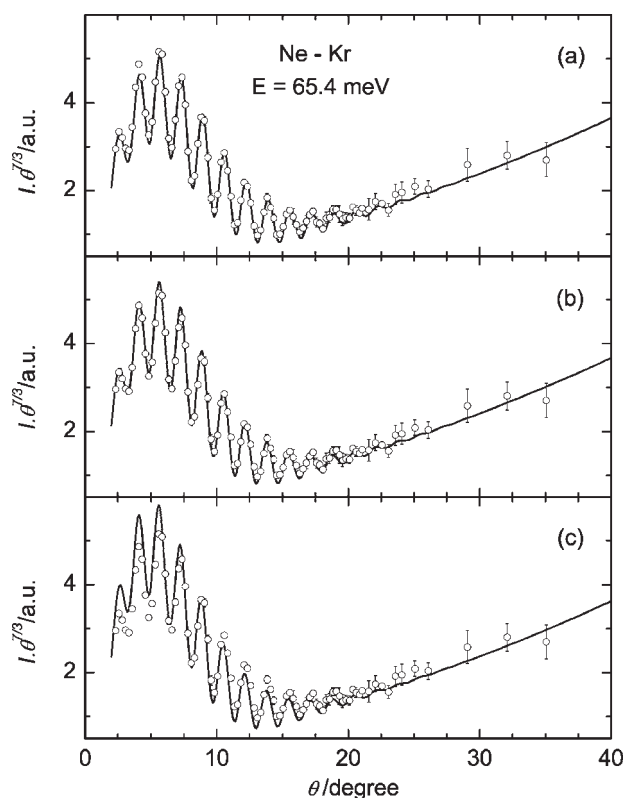


Fig. 10 $I(\theta)$ data at the collision energy E , multiplied by $\theta^{7/3}$ and plotted as a function of the laboratory scattering angle θ . Error bars are indicated when larger than the experimental dots. Comparison between experimental results and calculations (full lines) with HFD-B (a), ILJ (b) and LJ (c) models.

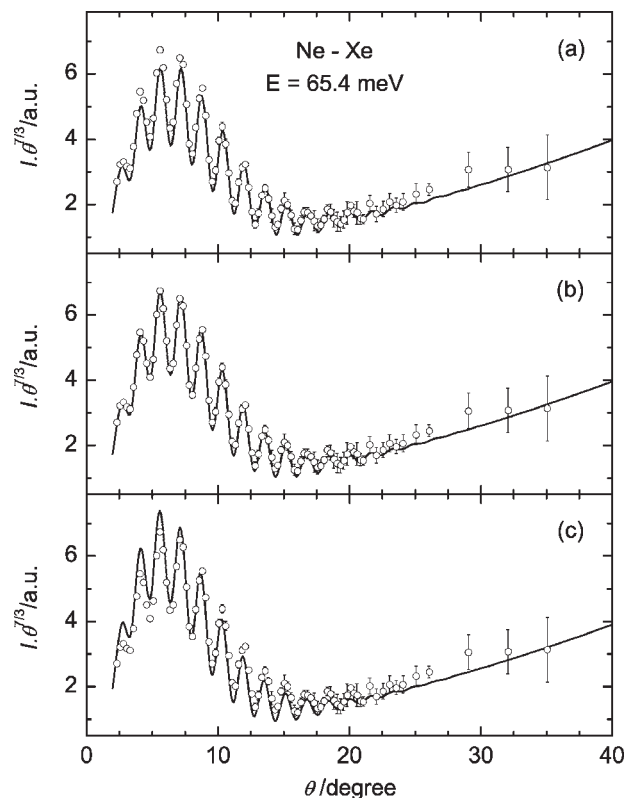


Fig. 12 $I(\theta)$ data at the collision energy E , multiplied by $\theta^{7/3}$ and plotted as a function of the laboratory scattering angle θ . Error bars are indicated when larger than the experimental dots. Comparison between experimental results and calculations (full lines) with HFD-B (a), ILJ (b) and LJ (c) models.

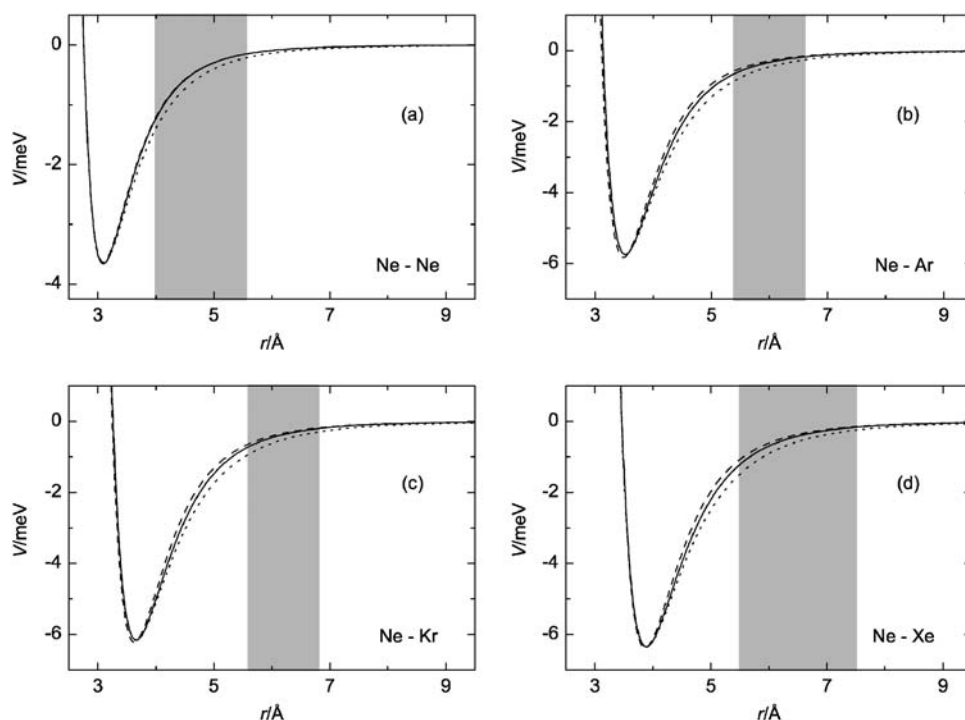


Fig. 13 Comparison between the interaction potential models in the well region and at long-range: ILJ (full lines), LJ (dotted lines) and HFD (dashed lines) models (see also Tables 2 and 3). The shaded region defines the r interval probed by the $\bar{Q}(v)$ values and where differences in the potential models are more effective.

a glory pattern in agreement with the experimental one, while the absolute value of $\bar{Q}(v)$ falls slightly outside the lower limit of the experimental uncertainty. The analysis of $I(\theta)$ indicates that the diffraction oscillations are well reproduced by all potentials since they exhibit similar σ values (see Table 2). However, the shape of the rainbow structure in the low θ range, which is partially affected by the scattering driven by the long-range attraction, is not described well by LJ (the intensity is overestimated since the LJ is too attractive) and is slightly underestimated by HFD-B.

As mentioned in section V, in the case of Ne–Xe scattering, the use of high-resolution conditions in our experiments permitted us to resolve two glory maxima and one glory minimum in the velocity dependence of the integral cross section (see Fig. 11). The differential cross sections have been plotted in Fig. 12 again as $I(\theta)\theta^{7/3}$. The simultaneous analysis, performed as for Ne–Ne, Ne–Ar and Ne–Kr, has involved the use of HFD-B, taken from,⁵⁵ LJ and ILJ potential models. In the ILJ case, r_m has been varied only within a limited range of values around the spectroscopic determination⁵⁶ and only ϵ has been considered as a completely free parameter in the best-fit procedure. It should also be noted that the diffraction oscillations provide an absolute determination of σ (within 0.6%), and indirectly of r_m (see ref. 48). The r_m value given in Table 2 agrees within 0.2% with the accurate spectroscopic value of r_m (3.879 Å).⁵⁶ Other considerations made above for Ne–Kr also apply to Ne–Xe. In particular, the $\bar{Q}(v)$ component appears to be overestimated by LJ and underestimated by HFD-B (see also caption to Fig. 11), and corresponding deviations in the $I(\theta)\theta^{7/3}$ behavior are again observed at low θ values (see Fig. 12).

The experimental scattering observables analyzed here are affected (see section III) by specific features of the potential well. For each system, Fig. 13 reports, in the well region and at long-range, the HFD-B, ILJ and LJ potentials to better compare similarities and differences in their shape. The shaded region defines the r interval ($[r_1, r_2]$, see Table 3) probed by the $\bar{Q}(v)$ value.^{44,57} The nearly correct reproduction of the $\Delta Q(v)$ glory pattern by the three potentials is due to the similarity of the interaction for $r \lesssim r_m$. Table 3 reports, for all the potential models used, some features of the long-range attraction at the distance r^* , mainly probed by $\bar{Q}(v)$ and intermediate between r_1 and r_2 ,^{44,57} and also at larger r . In particular, we have chosen $r/r_m = 5$, where only the dipole–dipole C_6 coefficient contributes to the attraction, the role of the higher dispersion coefficients being negligible, and $r \rightarrow \infty$, where the ILJ assumes the limiting value $C_6 = \epsilon r_m^6$. The C_6 values extrapolated by ILJ appear to be in agreement within 10% (only for Ne–Ne does the deviation amount to about 15%) with both theoretical and experimental C_6 values available from the literature.^{58,59} As expected, LJ(12,6) gives C_6 ($C_6 = 2\epsilon r_m^6$) larger by a factor of two. In all cases, the HFD-B models involve C_6 values fixed at the theoretical values⁵⁸ (further theoretical information on the dispersion coefficients are given in ref. 60 and 61).

VI. The Leiden experiments

Several years ago the Leiden laboratory reported integral cross section data for symmetric and asymmetric rare gas systems^{34,35} over an extended velocity range. The results were provided on a relative scale in the CM system. These data are

Table 3 Smallest (r_1), largest (r_2) and mainly probed distance (r^*) by the average component of the cross section $\bar{Q}(v)$. Reported data are in Å. The long-range interaction $V(r^*)$ is in meV. Dipole–dipole dispersion coefficients C_6 , in eVÅ⁶, provided by the ILJ model at different reduced values of the distance $x = r/r_m$, are compared with predictions of other potential models and with theoretical, C_{6th} ,⁵⁸ and experimental C_{6exp} results⁵⁹

System	Potential	r_1	r_2	r^*	$V(r^*)$	C_6 ($x = 5$)	C_6 ($x = \infty$)	C_{6th}	C_{6exp}
He–Xe ^a	ILJ	—	—	—	—	11.3	10.7	11.7	11.6
	LJ					21.3	21.3		
	HFD ^b					11.9	11.7		
	HFD ^c					11.9	11.7		
Ne–Ne	ILJ	4.0	5.6	4.8	−0.387	3.40	3.21	3.81	3.69
	LJ				−0.506	6.42	6.42		
	HFD-B ^d				−0.382	3.92	3.85		
	HFD-B ^e				−0.287	11.7	11.5		
Ne–Ar	ILJ	5.4	6.6	6.0	−0.325	11.6	10.9	11.7	11.5
	LJ				−0.458	21.8	21.8		
	HFD-B ^e				−0.287	11.7	11.5		
	HFD-B ^f				−0.329	16.4	16.1		
Ne–Kr	ILJ	5.6	6.8	6.2	−0.369	15.7	14.8	16.3	16.1
	LJ				−0.510	29.6	29.6		
	HFD-B ^e				−0.329	16.4	16.1		
	HFD-B ^f				−0.412	23.1	21.8	23.7	23.3
Ne–Xe	ILJ	5.5	7.5	6.5	−0.412	23.1	21.8	23.7	23.3
	LJ				−0.566	43.7	43.7		
	HFD-B ^e				−0.364	23.8	23.5		
	HFD-B ^f				−0.364	23.8	23.5		

^a For this system, r_1 , r_2 and r^* values are unavailable since $Q(v)$ has been measured in the intermediate velocity range (see text), where $Q(v)$ is not fully separable in an average and in an oscillatory component.

^b Ref. 52. ^c Ref. 51. ^d Ref. 53. ^e Ref. 54. ^f Ref. 55.

also included in the present analysis. The integral cross sections measured in Leiden are plotted in Fig. 14 as $Q(g)g^{2/5}$, where they are compared with the calculations performed using the ILJ model. The glory undulatory structure $\Delta Q(g)$ is well evident in all systems and, although in relative scale, the smooth $\bar{Q}(g)$ component is provided in a wide g range.

For Ne–Ar, Ne–Kr and Ne–Xe the $Q(g)$ calculations have been performed with the parameters of Table 2. In the cases of heavier rare gas systems, r_m has been taken in the range provided by spectroscopic information^{56,62–64} and only ϵ has been varied freely. The best-fit potential parameters are reported in Table 4, where they are again compared with the predictions of our correlation formulae. Fig. 14 shows that ILJ reproduces both amplitude and frequency of the $\Delta Q(g)$ pattern. Therefore, this analysis represents a further test of the accuracy of the description of the interaction for $r \lesssim r_m$.^{41,44,65–67} Moreover, the $\bar{Q}(g)$ component does not exhibit a pure $g^{2/5}$ dependence⁴⁴ and thus it provides an important probe of the long-range $C_6(r)$ function involved in the model. Indeed, this term represents an effective long-range C_6 coefficient, including the contribution of the induced dipole–induced dipole component and of higher order dispersion damped terms, whose relative importance varies with r . Moreover, the comparison between the C_6 term, provided by ILJ at different reduced distances r/r_m , with theoretical and experimental results (see Table 5), confirms the good description of the long-range attraction also for heavier rare gas systems.

Fig. 15 (upper panel), shows the experimental integral cross section data for the Ar–Ar system, together with the results of calculations performed by using the best-fit ILJ, and as usual, the LJ with the same ϵ and r_m . The comparison demonstrates that the slope predicted by LJ shows some deviation from the

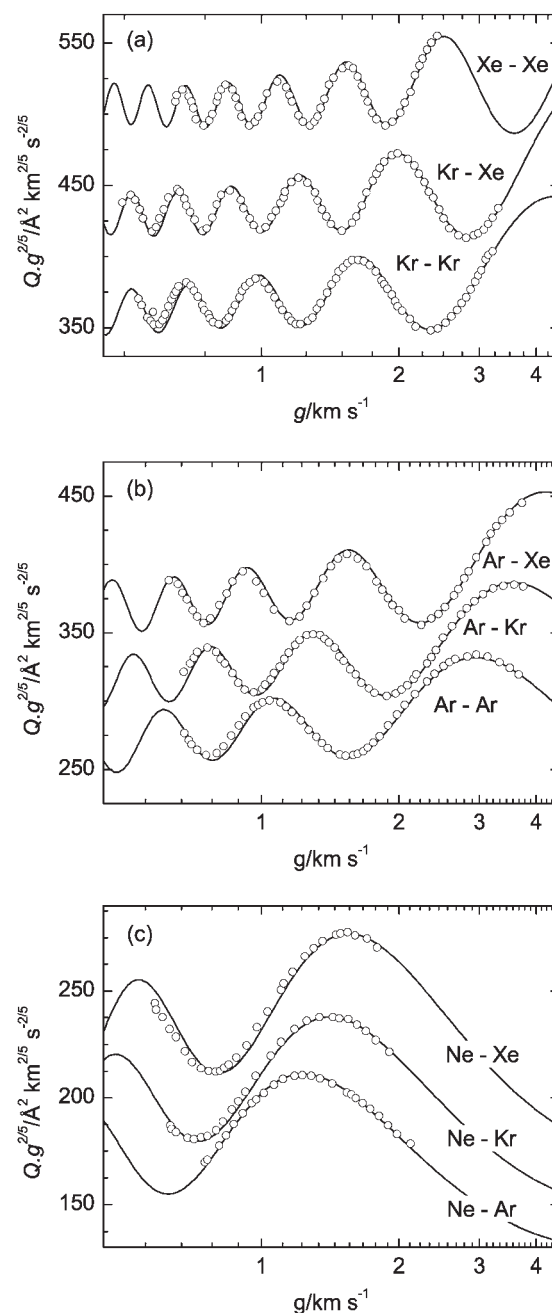


Fig. 14 Integral cross sections $Q(g)$, measured in the Leiden laboratory for several rare gas-rare gas systems, plotted as a function of the relative velocity g . The full lines are the calculations performed with the ILJ model.

experimental one, due to its C_6 coefficient being independent from r . The lower panel presents a comparison between vibrational levels supported by ILJ and LJ. Differences in their energies can again be, for the major part, ascribed to the different long-range behavior of the two models.

VII. Discussion

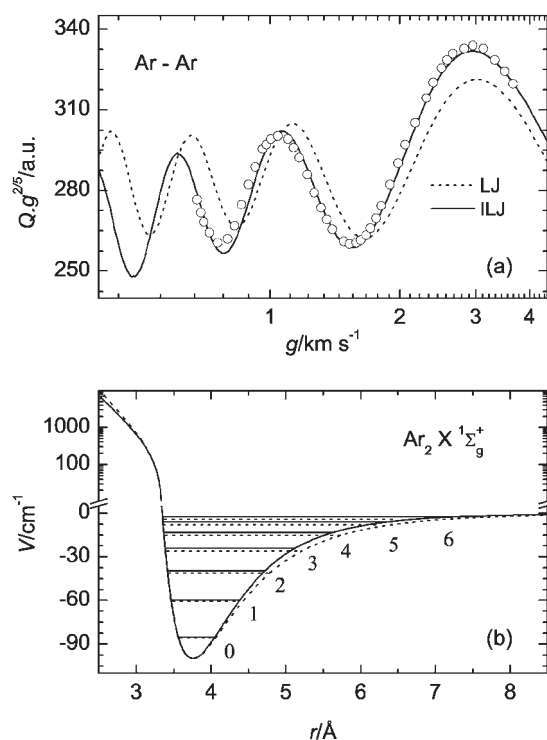
In the previous sections we focused our attention on the analysis of scattering properties, including quantum interference effects, and on their dependence on specific features of the

Table 4 Well depth ε , equilibrium distance r_m and zero of the potential σ for ILJ compared with predictions of correlation formulae

System	Model potential	ε/meV	$\sigma/\text{\AA}$	$r_m/\text{\AA}$
Ar–Ar	ILJ	12.370	3.350	3.757
	Predicted ^a	11.61		3.79
Ar–Kr	ILJ	14.330	3.483	3.910
	Predicted ^a	14.08		3.92
Ar–Xe	ILJ	16.090	3.652	4.100
	Predicted ^a	15.92		4.09
Kr–Kr	ILJ	17.300	3.576	4.010
	Predicted ^a	17.61		4.03
Kr–Xe	ILJ	19.950	3.741	4.200
	Predicted ^a	20.63		4.18
Xe–Xe	ILJ	24.200	3.879	4.350
	Predicted ^a	25.36		4.32

^a Ref. 49 and 50.**Table 5** Dipole–dipole dispersion coefficients C_6 , in $\text{eV}\text{\AA}^6$, provided by the ILJ model at different reduced distance $x = r/r_m$ values, compared with theoretical, $C_{6\text{th}}$,⁵⁸ and experimental $C_{6\text{exp}}$ results,⁵⁹ for the heavier symmetric and asymmetric rare gas–rare gas systems

System	$C_6(x=5)$	$C_6(x=\infty)$	$C_{6\text{th}}$	$C_{6\text{exp}}$
Ar–Ar	36.8	34.8	38.4	38.5
Ar–Kr	54.2	51.2	54.5	54.4
Ar–Xe	80.9	76.4	80.4	80.1
Kr–Kr	76.1	71.9	77.4	77.2
Kr–Xe	116	110	115	114
Xe–Xe	174	164	171	170

**Fig. 15** Upper panel: the integral cross sections Q for the Ar–Ar system measured in the Leiden laboratory, compared with calculations performed using ILJ (full line) and LJ (dotted line). Lower panel: vibrational levels supported by ILJ and LJ potentials.

interaction potential $V(r)$ (see Fig. 2). Such an analysis represents an important and critical probe of the ILJ model on the rare gas–rare gas systems, and especially concerns its ability to describe both the long-range attraction and the potential well. As a further test of such an ability, for symmetric systems we have also performed the calculation of the vibrational levels by using the first-order WKB quantum condition of $V(r)$ eigenvalues, and have then compared the computed energy spacings with the spectroscopic results.^{8–13} The comparison is shown in Table 6 and demonstrates that, although no fitting procedure has been adopted, the predictions are in reasonable agreement with the experimental data (often within the quoted uncertainties).

As already discussed in section IV, the $n(r)$ dependence in the ILJ model leads to a correct description of $V(r)$ at intermediate and large r . Moreover, the $n(r)$ dependence also reduces the hardness of the repulsive wall with respect to that of the familiar LJ(12,6) model. Although the ILJ probably still remains too repulsive for $r \rightarrow 0$, its behavior in the first repulsive part close to σ appears to be very reliable, as can be appreciated from its ability to well reproduce the detailed diffraction oscillation pattern observed experimentally in the differential cross sections, which is very sensitive to σ and to the slope of the low repulsive part of the potential. Here, the reliability of the first repulsive part is further tested by comparing the ILJ potential behavior with the energy values obtained for several systems from the inversion of gaseous transport coefficients.⁷ This comparison is shown in Fig. 16. In general, the agreement appears to be quite good confirming the correctness of the ILJ description also at $r < \sigma$.

Table 6 Comparison of experimental and calculated vibrational energy spacings (cm^{-1}) for the symmetric rare gas systems. Experimental uncertainties range between a few hundredths of cm^{-1} and 0.75 cm^{-1}

Molecule	$\nu' - \nu''$	Experiment	ILJ Potential
Ne ₂	1–0	13.70 ^a	13.94
	1–0	25.74 ^b	25.34
Ar ₂	2–1	20.41	20.32
	3–2	15.61	15.52
	4–3	10.90	11.06
Kr ₂	5–4	6.78	7.13
	1–0	21.18 ^c	21.17
	2–1	19.09	19.02
	3–2	16.76 ^d	16.90
	4–3	14.76	14.83
Xe ₂	5–4	12.23	12.82
	6–5	10.49	10.87
	7–6	8.92	9.01
	8–7	6.92	7.26
	9–8	5.54	5.65
	1–0	19.90 ^e	19.15
	2–1	18.55	17.98
	3–2	17.20	16.81
	4–3	16.17	15.65
	5–4	14.63	14.52
	6–5	13.70	13.39
	7–6	12.63	12.28
	8–7	11.33	11.20
	9–8	10.15	10.13
	10–9	8.95	9.09

^a Ref. 8. ^b Ref. 11. ^c Ref. 12. ^d Ref. 9. ^e Ref. 10.

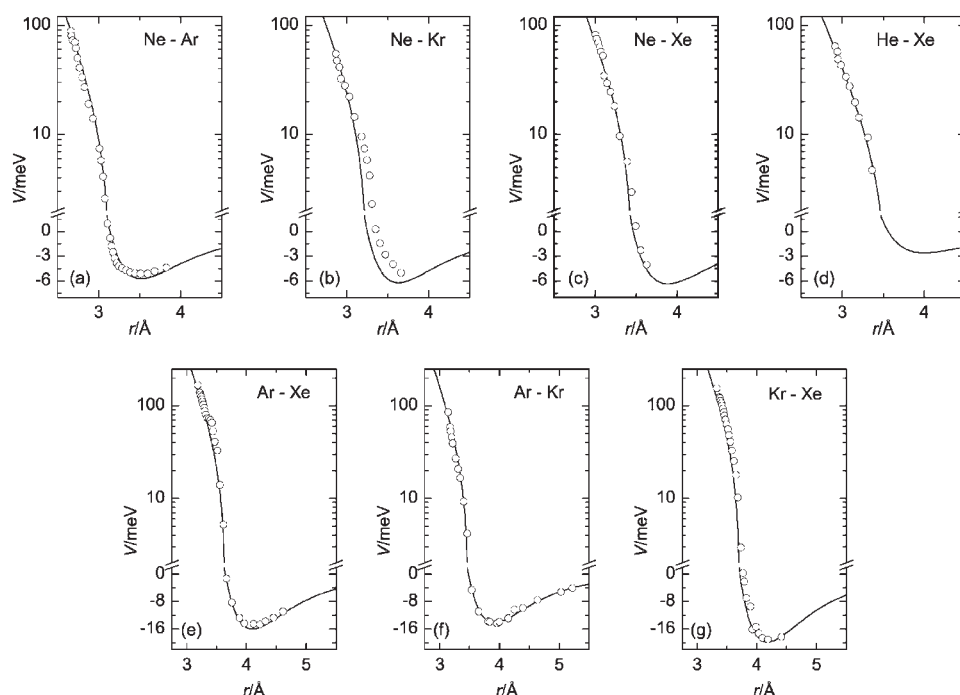


Fig. 16 Interatomic potential energies for several rare gas-rare gas systems. The full lines represent the results of ILJ. The circles are the energies obtained by the inversion of gaseous transport coefficients.⁷

As stressed above, V_{vdW} is a basic component of non-covalent interactions. These can often include other important contributions when systems different from rare gas-rare gas dimers are considered. In particular, induction and electrostatic contributions can appear at large r , while charge transfer effects can emerge as r decreases.³² Therefore, the representation of the non-covalent interactions requires both the correct evaluation of all these contributions and the proper

formulation of the resulting intermolecular potential. Here, the crucial question concerns the assessment of potentialities and limitations of the generalized use of ILJ. For this reason, the present investigation is also extended to systems involving ions. To this purpose, we chose three prototypical systems, namely $\text{K}^+\text{-Ar}$, $\text{Cl}^-\text{-Ar}$ and $\text{K}^+\text{-Cl}^-$, whose interaction potentials have been investigated in detail elsewhere by coupling experimental and theoretical information.^{68–70} Fig. 17

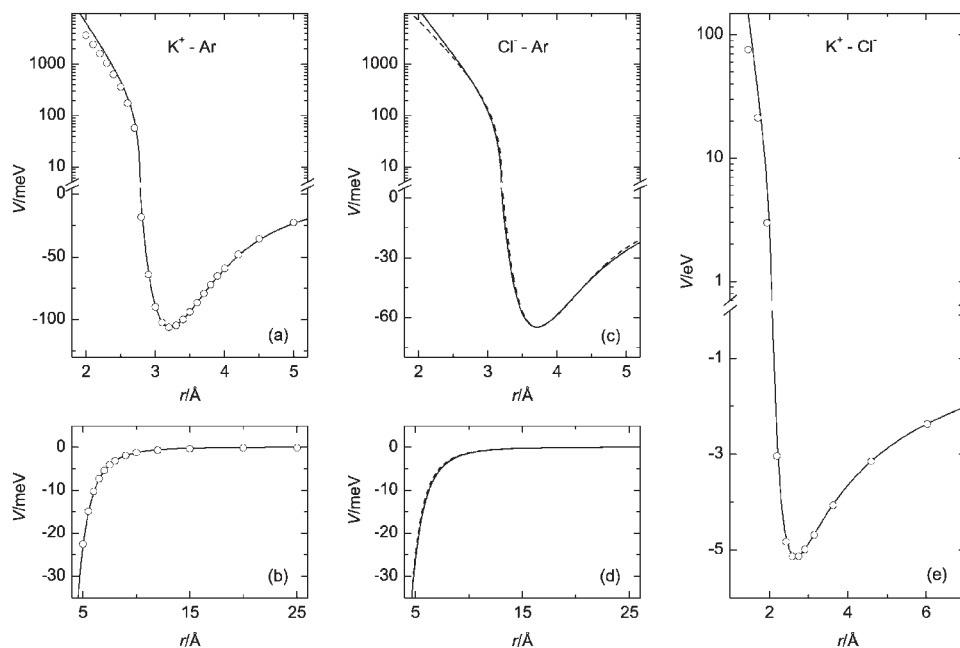


Fig. 17 Comparison between $V(r)$ values provided by ILJ (full lines) and results from the literature. Open circles are results from ref. 68 and 70; dashed line represents the potential given in ref. 69.

Table 7 ILJ potential parameters for some systems involving closed-shell ions and comparison with predictions of correlations formulae

System	Potential	β	ε/meV	$r_m/\text{\AA}$
K^+-Ar	ILJ	8.4	106.158	3.215
	Predicted ^a		110.0	3.19
Cl^--Ar	ILJ	7.8	64.870	3.710
	Predicted ^a		76.0	3.77
K^+-Cl^-	ILJ	8.0	5154	2.667
	Predicted ^b		5160	2.65

^a Ref. 71. ^b Ref. 72.

shows a comparison between $V(r)$ provided by the ILJ model and results from the literature.^{68–70} In particular, for K^+-Ar and Cl^--Ar the m exponent in the second term of eqn (4.2) has been fixed to $m = 4$, since in these systems the leading interaction component at long-range is the induction, while $m = 1$ has been chosen for the K^+-Cl^- case, where the charge–charge electrostatic contribution dominates the asymptotic attraction. The potential parameters for the three systems are given in Table 7, where they are compared with predictions of correlation formulae given in terms of polarizability and charge of the interacting partners.^{71,72} For K^+-Ar and Cl^--Ar , the accuracy of the long-range attraction description is well evident in the lower panels of Fig. 17, while for K^+-Cl^- , the asymptotic charge–charge constant, $C_1 = \varepsilon r_m = 13.75 \text{ eV/\AA}$, appears to deviate from the single charge–single charge Coulomb constant ($C_1 = 14.40 \text{ eV/\AA}$) by only 4.5%. It is also important to stress the closeness of the β value for various systems ($\beta = 9$ for all the rare gas–rare gas pairs must be compared with the data in Table 7) and its attenuated dependence on the hardness of the involved partners.⁷³

The analysis of the ionic systems confirms that the ILJ model can cover a wide range of phenomenology. In addition, the combined use of the ILJ model and correlation formulae, providing ε and r_m parameters for interacting partners of different nature, allows a reliable prediction of $V(r)$ for a large variety of systems, which may be difficult to characterize both experimentally and theoretically.

VIII. Conclusions and future directions

We have reported a detailed and important accuracy test of the ILJ potential model by using results of scattering experiments on rare gas–rare gas systems, *i.e.* systems that interact with pure van der Waals forces. These experiments have been performed under high-resolution conditions, in order to clearly resolve in the measured cross sections all of the quantum interference effects which are very sensitive to fine details of the interaction potential. We have demonstrated that the ILJ permits us to cover a wide range of phenomenologies, including systems with positive and negative ions. This offers us the perspective of an evaluation of the interaction properties in systems exhibiting an increasing complexity and in turn makes it possible to calculate equilibrium and non-equilibrium properties for systems of great practical interest, some of which are highlighted below.

A first example concerns the study of the H_2O , H_2S and NH_3 -rare gas systems, where other contributions can add to

V_{vdw} , especially when heavier rare gas atoms are involved, determining embryonic hydrogen bonds.⁷⁴ A second example regards the representation of anisotropic potentials in molecule–molecule systems and the study of energy transfer processes. The case of diatom–diatom complexes, represented as a bond–bond pair and including the dependence of the intermolecular interaction from the bond orientation and bond length, has been recently investigated.⁷⁵ Studies of the transition from water clusters to liquid water and of solvation phenomena are also in progress.

An immediate application presented here is the evaluation of the resulting potential well depth D controlling the physical absorption of gaseous species on a graphite monolayer. In particular, we have exploited the atom–bond pairwise additive approach,³⁰ which directly includes three-body effects, differently from the familiar atom–atom pairwise representation. The atom–bond potential parameters have been estimated from the polarizability components of the C–C bond, evaluated from its bond-order and bond-length in graphite (slightly different with respect to the C–C bond in the benzene molecule^{30,76}). Following guidelines given previously,³⁰ for any orientation angle γ of the atom–bond pair the potential parameters are defined as

$$r_m(\gamma) = r_{m\parallel}\cos^2(\gamma) + r_{m\perp}\sin^2(\gamma)$$

$$\varepsilon(\gamma) = \varepsilon_{\parallel}\cos^2(\gamma) + \varepsilon_{\perp}\sin^2(\gamma). \quad (8.5)$$

This allows us to introduce the dependence on γ in eqns (4.2) and (4.3). The values of $r_{m\parallel}$, $r_{m\perp}$, ε_{\parallel} and ε_{\perp} for rare gases, H_2 (considered as pseudoatom) and H are given in Table 8. The results of this evaluation concerning the resulting well depth D , associated to the interaction of each species with a graphite monolayer, are reported in the same table. They compare well with the best estimates given in ref. 77, considering both the uncertainty of correlation formulae used for the prediction of the potential parameters and that of the estimated values.

As a final consideration, it has to be emphasized again the importance of performing accurate molecular dynamics simulations to understand and control the features of equilibrium and non-equilibrium states of matter, such as solvation phenomena and their dependence on environmental conditions,⁷⁸ the behavior of highly unstable species in plasmas⁷⁹ and the main characteristics of planetary atmospheres and of associated transport phenomena.^{73,80} In these simulations, in order to be able to actually perform the calculations, the treatment

Table 8 ILJ potential parameters (ε in meV, r_m in \AA and $\beta = 8.0$) used to calculate the well depth D , for the interaction of several species with a graphite monolayer, and comparison with values from the literature

Species	ε_{\parallel}	ε_{\perp}	$r_{m\parallel}$	$r_{m\perp}$	D (predicted)	D^a
He	0.866	0.721	3.936	3.536	19.5	16.6
Ne	1.809	1.418	3.995	3.589	40.6	32.6
Ar	4.608	3.144	4.147	3.851	103.4	96
Kr	5.906	3.864	4.249	3.974	136.2	125
Xe	7.195	4.484	4.397	4.145	173.3	162
H	1.733	1.293	4.000	3.660	37.9	43
H_2	2.281	1.674	4.021	3.689	50.0	51.7

^a Ref. 77.

of the molecular dynamics requires the use of simple and reliable (*i.e.* physically accurate) functions for the representation of $V(r)$ (see, for instance, ref. 81), preferentially formulated in terms of a few parameters, having a direct physical meaning. As this paper shows, the ILJ model completely meets these requirements and may become widely used in molecular dynamics simulations, since it provides, with respect to the familiar LJ a more accurate representation of the intermolecular interaction with only a small increase in computational time.

Acknowledgements

The work has been supported by the Italian Ministero della Università e Ricerca (MIUR) through PRIN's and FIRB's contracts. Luiz F. Roncaratti acknowledges the Alban Programme scholarship. We thank L. Beneventi for the experimental contribution to part of this work and V. Aquilanti, G. Liuti and G. G. Volpi for useful discussions and continuous support.

References

- G. C. Maitland, M. Rigby, E. B. Smith and W. A. Wakeham, in *Intermolecular Forces: Their origin and determination*, Clarendon Press, Oxford, 1987.
- J. M. Farrar, Y. T. Lee, V. V. Goldman and M. L. Klein, *Chem. Phys. Lett.*, 1973, **19**, 359.
- C. Y. Ng, Y. T. Lee and J. A. Barker, *J. Chem. Phys.*, 1974, **61**, 1996.
- B. Brunetti, R. Cambi, F. Pirani, F. Vecchiocattivi and M. Tomassini, *Chem. Phys.*, 1979, **42**, 397.
- R. A. Aziz, P. W. Riley, U. Buck, G. Maneke, J. Schleusener, G. Scoles and U. Valbusa, *J. Chem. Phys.*, 1979, **71**, 2637.
- R. Candori, F. Pirani and F. Vecchiocattivi, *Mol. Phys.*, 1983, **49**, 551.
- G. C. Maitland and W. A. Wakeham, *Mol. Phys.*, 1978, **35**, 1443.
- Y. Tanaka and K. Yoshino, *J. Chem. Phys.*, 1972, **57**, 2964.
- Y. Tanaka, K. Yoshino and D. E. Freeman, *J. Chem. Phys.*, 1973, **59**, 5160.
- D. E. Freeman, K. Yoshino and Y. Tanaka, *J. Chem. Phys.*, 1974, **61**, 4880.
- E. A. Colbourn and A. E. Douglas, *J. Chem. Phys.*, 1976, **65**, 1741.
- P. E. Larocque, R. H. Lipson, P. R. Herman and B. P. Stoicheff, *J. Chem. Phys.*, 1986, **85**, 6627.
- P. R. Herman, P. E. Larocque and B. P. Stoicheff, *J. Chem. Phys.*, 1988, **89**, 4535.
- G. Scoles, *Annu. Rev. Phys. Chem.*, 1980, **31**, 81.
- R. A. Aziz, in *Inert Gases*, Springer Series in Chemical Physics, ed. M. Klein, Springer, Berlin, 1984, vol. 34.
- P. E. Siska, J. M. Parson, T. P. Schafer and Y. T. Lee, *J. Chem. Phys.*, 1971, **55**, 5672.
- G. Simons, R. G. Parr and J. M. Finlan, *J. Chem. Phys.*, 1973, **59**, 3229.
- R. W. Bickes and R. B. Bernstein, *Chem. Phys. Lett.*, 1974, **26**, 457.
- R. W. Bickes and R. B. Bernstein, *J. Chem. Phys.*, 1977, **66**, 2408.
- J. Hepburn, R. Penco and G. Scoles, *Chem. Phys. Lett.*, 1975, **36**, 451.
- R. Ahlrichs, R. Penco and G. Scoles, *Chem. Phys.*, 1977, **19**, 152.
- R. A. Aziz and H. H. Chen, *J. Chem. Phys.*, 1977, **67**, 5719.
- C. Douketis, G. Scoles, S. Marchetti, M. Zen and A. J. Thakkar, *J. Chem. Phys.*, 1982, **76**, 3057.
- R. A. Aziz, W. J. Meath and A. R. Allnatt, *Chem. Phys.*, 1983, **78**, 295.
- A. K. Dham, A. R. Allnatt, W. J. Meath and R. A. Aziz, *Mol. Phys.*, 1989, **67**, 1291.
- K. T. Tang and J. P. Toennies, *J. Chem. Phys.*, 1984, **80**, 3726.
- R. Ahlrichs, H. J. Böhm, S. Brode, K. T. Tang and J. P. Toennies, *J. Chem. Phys.*, 1988, **88**, 6290.
- C. Nyeland and J. P. Toennies, *Chem. Phys.*, 1988, **122**, 337.
- J. E. Lennard-Jones, *Proc. R. Soc. London, Ser. A*, 1924, **106**, 463.
- F. Pirani, M. Alberti, A. Castro, M. Moix Teixidor and D. Cappelletti, *Chem. Phys. Lett.*, 2004, **394**, 37.
- G. C. Maitland and E. B. Smith, *Chem. Phys. Lett.*, 1973, **22**, 443.
- F. Pirani, G. S. Maciel, D. Cappelletti and V. Aquilanti, *Int. Rev. Phys. Chem.*, 2006, **25**, 165.
- K. T. Tang and J. P. Toennies, *J. Chem. Phys.*, 2003, **118**, 4976.
- J. J. H. van den Biesen, Ph.D. Thesis, Leiden University, 1982.
- J. J. H. van den Biesen, R. M. Hermans and C. J. N. van den Meijdenberg, *Physica A*, 1982, **115**, 396.
- D. Cappelletti, M. Bartolomei, F. Pirani and V. Aquilanti, *J. Phys. Chem. A*, 2002, **106**, 10764.
- D. Cappelletti, V. Aquilanti, E. Cornicchi, Marc Moix Teixidor and F. Pirani, *J. Chem. Phys.*, 2005, **123**, 024302.
- L. Beneventi, P. Casavecchia and G. G. Volpi, *J. Chem. Phys.*, 1986, **85**, 7011.
- L. Beneventi, PhD Thesis, University of Perugia, 1990; L. Beneventi, P. Casavecchia and G. G. Volpi, in *Electronic and Atomic Collisions*, ed. W. R. MacGillivray, I. E. McCarthy and M. C. Standage, Adam Hilger, New York, 1992, pp. 527–536.
- V. Aquilanti, D. Cappelletti, V. Lorent, E. Luzzatti and F. Pirani, *Chem. Phys. Lett.*, 1992, **192**, 153.
- R. B. Bernstein, *Adv. Chem. Phys.*, 1966, **10**, 75.
- U. Buck, *Rev. Mod. Phys.*, 1974, **46**, 369.
- U. Buck, *Adv. Chem. Phys.*, 1975, **30**, 313; U. Buck, in *Atomic and Molecular Beam Methods*, ed. G. Scoles, New York–Oxford, 1987, vol. 1.
- F. Pirani and F. Vecchiocattivi, *Mol. Phys.*, 1982, **45**, 1003.
- D. W. Gough, E. B. Smith and G. C. Maitland, *Mol. Phys.*, 1974, **27**, 867.
- B. Brunetti, E. Luzzatti, F. Pirani and F. Vecchiocattivi, *Chem. Phys. Lett.*, 1978, **58**, 504.
- R. Candori, F. Pirani and F. Vecchiocattivi, *Chem. Phys. Lett.*, 1982, **90**, 202; R. Candori, F. Pirani and F. Vecchiocattivi, *J. Chem. Phys.*, 1986, **84**, 4833.
- L. Beneventi, P. Casavecchia and G. G. Volpi, *J. Chem. Phys.*, 1986, **84**, 4828.
- G. Liuti and F. Pirani, *Chem. Phys. Lett.*, 1985, **122**, 245.
- R. Cambi, D. Cappelletti, G. Liuti and F. Pirani, *J. Chem. Phys.*, 1991, **95**, 1852.
- L. J. Danielson and M. Keil, *J. Chem. Phys.*, 1988, **88**, 851.
- R. A. Aziz, U. Buck, H. Jónsson, J.-C. Ruiz-Suárez, B. Schmidt, G. Scoles, M. J. Slaman and J. Xu, *J. Chem. Phys.*, 1989, **91**, 6477.
- R. A. Aziz and M. J. Slaman, *Chem. Phys.*, 1989, **130**, 187.
- D. A. Barrow and R. A. Aziz, *J. Chem. Phys.*, 1988, **89**, 6189.
- D. A. Barrow, M. J. Slaman and R. A. Aziz, *J. Chem. Phys.*, 1989, **91**, 6348.
- W. Jäger, Y. Xu and M. C. L. Gerry, *J. Chem. Phys.*, 1993, **99**, 919.
- P. Dehmer and L. Wharton, *J. Chem. Phys.*, 1972, **57**, 4821.
- A. Kumar and W. J. Meath, *Mol. Phys.*, 1985, **54**, 823.
- T. N. Olney, N. M. Cann, G. Cooper and C. E. Brion, *Chem. Phys.*, 1997, **223**, 59.
- J. M. Standard and P. R. Certain, *J. Chem. Phys.*, 1985, **83**, 3002.
- A. J. Thakkar, H. Hettema and P. E. S. Wormer, *J. Chem. Phys.*, 1992, **97**, 3252.
- J. F. Ogilvie and Frank Y. H. Wang, *J. Mol. Struct.*, 1992, **273**, 277.
- J. F. Ogilvie and Frank Y. H. Wang, *J. Mol. Struct.*, 1993, **291**, 313.
- R. A. Aziz, *J. Chem. Phys.*, 1993, **99**, 4518.
- R. B. Bernstein and T. J. P. O'Brien, *J. Chem. Phys.*, 1967, **46**, 1208.
- E. F. Greene and E. A. Mason, *J. Chem. Phys.*, 1972, **57**, 2065.
- E. F. Greene and E. A. Mason, *J. Chem. Phys.*, 1973, **59**, 2651.
- L. A. Viehland, J. Lozeille, P. Soldán, E. P. F. Lee and T. G. Wright, *J. Chem. Phys.*, 2004, **121**, 341.
- T. Lenzer, I. Yourshaw, M. R. Furlanetto, G. Reiser and D. M. Neumark, *J. Chem. Phys.*, 1999, **110**, 9578.
- S. H. Patil, *J. Chem. Phys.*, 1987, **86**, 313.
- D. Cappelletti, G. Liuti and F. Pirani, *Chem. Phys. Lett.*, 1991, **183**, 297.

-
- 72 V. Aquilanti, D. Cappelletti and F. Pirani, *Chem. Phys.*, 1996, **209**, 299.
- 73 M. Capitelli, D. Cappelletti, G. Colonna, C. Gorse, A. Laricchiuta, G. Liuti, S. Longo and F. Pirani, *Chem. Phys.*, 2007, **339**, 62.
- 74 V. Aquilanti, E. Cornicchi, M. Moix Teixidor, N. Saendig and F. Pirani, *Angew. Chem., Int. Ed.*, 2005, **44**, 2356.
- 75 D. Cappelletti, F. Pirani, B. Bussery-Honvault, L. Gomes and M. Bartolomei, *Phys. Chem. Chem. Phys.*, 2008, **10**, 4281.
- 76 M. Alberti, A. Castro, A. Laganà, M. Moix Teixidor, F. Pirani, D. Cappelletti and G. Liuti, *J. Phys. Chem. A*, 2005, **109**, 2906.
- 77 G. Vidali, G. Ihm, H. Y. Kim and M. W. Cole, *Surf. Sci. Rep.*, 1991, **12**, 133.
- 78 M. Alberti, A. Aguilar, J. M. Lucas, A. Laganà and F. Pirani, *J. Phys. Chem. A*, 2007, **111**, 1780.
- 79 P. Candori, S. Falcinelli, F. Pirani, F. Tarantelli and F. Vecchiocattivi, *Chem. Phys. Lett.*, 2007, **436**, 322.
- 80 A. Laricchiuta, D. Bruno, C. Catalfamo, F. Pirani, G. Colonna, P. Diomede, D. Pagano, C. Gorse, S. Longo, R. Celiberto and M. Capitelli, *AIAA Proceedings 39th Thermophysics Conference*, Miami, 2007.
- 81 B. Guillot, *J. Mol. Liq.*, 2002, **101**, 219.